In situ measurement of bulk modulus and yield response of glassy thin films via confined layer compression

Owen Brazil[1] , Johann P. de Silva[1], Mithun Chowdhury[1,b)], Heedong Yoon[2], Gregory B. McKenna[2], Warren C. Oliver[3], Jason Kilpatrick[4], John B. Pethica[1], Graham L.W. Cross[5,a)]

[1]School of Physics, CRANN & AMBER, Trinity College, Dublin 2, Ireland
[2]Department of Chemical Engineering, Texas Tech University, Lubbock, Texas 79409-3121, USA
[3]Nanomechanics Inc., KLA-Tencor, Oak Ridge, Tennessee 37830, USA
[4]Adama Innovations Ltd., CRANN, Trinity College, Dublin 2, Ireland
[5]School of Physics, CRANN & AMBER, Trinity College, Dublin 2, Ireland;
and Adama Innovations Ltd., CRANN, Trinity College, Dublin 2, Ireland
a)Address all correspondence to this author. e-mail: graham.cross@tcd.ie
b)Present address: Metallurgical Engineering and Materials Science, Indian Institute of Technology Bombay, Mumbai 400076, India.

The measurement of thin film mechanical properties free from substrate influence remains one of the outstanding challenges in nanomechanics. Here, a technique based on indentation of a supported film with a flat punch whose diameter is many times the initial film thickness is introduced. This geometry generates a state of confined uniaxial strain for material beneath the punch, allowing direct access to intrinsic stress versus strain response. For simple elastic–plastic materials, this enables material parameters such as elastic modulus, bulk modulus, Poisson's ratio, and yield stress to be simultaneously determined from a single loading curve. The phenomenon of confined plastic yield has not been previously observed in thin films or homogeneous materials, which we demonstrate here for 170 -470 nm thick polystyrene (PS), polymethyl-methacrylate (PMMA) and amorphous Selenium films on silicon. As well as performing full elastic -plastic parameter extraction for these materials at room temperature, we used the technique to study the variation of yield stress in PS to temperatures above the nominal glass transition of 100 °C.

Supported thin films and bonded coatings are critical to both fabrication and function in many technologies, as well as allowing for fundamental scientific study of size and boundary effects brought about by reduced dimensionality in materials [1, 2]. However, efforts to measure their mechanical constitutive character remain challenging despite decades of theoretical and experimental efforts. Nanoindentation with sharp, self-similar tip geometries constitutes the primary mechanical characterization technique at submicron length scales [3, 4] but suffers from two significant drawbacks in regard to thin film testing; as a consequence of the contact geometry, access to intrinsic stress–strain response is extremely limited and there exists significant and complex convolution of the film response with that of the substrate [5, 6]. Efforts to alleviate these

problems typically involve labor-intensive geometric refinement of the sample [7, 8, 9], which may introduce further complications such as additional free surfaces and physically unrealistic geometries. Herein, we show that using a cylindrical flat punch indenter whose diameter is many times the initial film thickness, the intrinsic constitutive behavior of compliant films on stiffer substrates may be obtained, including a discrete elastic to plastic yield event. This enables straightforward access to stress versus strain data with no additional sample preparation required. This is made possible through the generation of a state of compressive *uniaxial strain* for material confined beneath the punch.

In macroscopic mechanical testing, the most commonly used deformation mode is the tensile/compressive uniaxial stress test, where a specimen is machined to a simple geometry of known dimensions and then stretched/compressed axially. A two-dimensional sketch of the compressive form is shown in Fig. 1(a). The application of an axial stress σ_{zz} results in the generation of a compressive axial strain ε_{zz} and lateral radial

---

*This article has been corrected since its original publication. An erratum notice detailing these changes was also published (doi: 10.1557/jmr.2020.67)

strains ε_{rr} through the Poisson effect in the elastic limit and through plastic shear flow following yield. A far less commonly utilized testing geometry is that of uniaxial strain, where a rigid confining jacket is placed snugly around the sample preventing any lateral expansion under an imposed axial stress, as shown in Fig. 1(b). For an isotropic linear elastic material undergoing uniaxial strain, the principal stress–strain relations are defined as [10] follows:

$$\sigma_{zz} = E\frac{(1-\nu)}{(1+\nu)(1-2\nu)}\varepsilon_{zz} = M\varepsilon_{zz} \quad , \qquad (1a)$$

$$\sigma_{rr} = \left(\frac{\nu}{1-\nu}\right)\sigma_{zz} \quad , \qquad (1b)$$

$$\varepsilon_{rr} = \varepsilon_{\theta\theta} = 0 \quad , \qquad (1c)$$

where E is Young's elastic modulus, ν is Poisson's ratio, and M is referred to as the confined elastic modulus (or the p-wave modulus in geomechanics [10].) With the addition of plastic constitutive behavior described by the von Mises criterion, where yield takes place at an axial stress Y_0 in unconfined uniaxial stress compression [Fig. 1(a)], yield in uniaxial strain occurs at a higher value of $Y_c = Y_0(1 - \nu)/(1 - 2\nu)$ due to lateral constraint. This value is referred to as the confined yield stress. Under the assumption of perfect plasticity, further loading past the yield stress in uniaxial strain results in a purely hydrostatic deformation as the yielding material can accumulate no further elastic shear, leading the stress–strain curve to adopt a new linear slope K, the elastic bulk modulus. Derivation of these stress–strain relations and the confined yield condition are included in the Supplementary material.

The constitutive behavior described above is summarized in Fig. 1(c). Of particular interest, the explicit relationship between stress and strain beyond the plastic yield limit due to confinement allows new information to be obtained from uniaxial strain generally not accessible due to unconstrained flow occurring in a conventional compression test. As well as allowing for measurement of K, Poisson's ratio may be determined via the following relationship:

$$\nu = \frac{3K - M}{3K + M} \quad . \qquad (2)$$

Outside of the geomechanics community, where it is commonly used to probe porous granular materials such as sands and soils [11], uniaxial strain testing has been seldom used, largely due to the high demands placed on support system rigidity and boundary conditions when testing macroscopic sample moduli at the GPa level [12, 13]. The favorable scaling of stiffness between sample and support instrument for microscale contacts, however, suggests that such a deformation mode may be realizable for thin films through the use of a flat punch indenter at a high punch diameter to film thickness aspect ratio. A sketch of our experiment is provided in Fig. 2(a). Using a dual-axis micro-positioning tilt stage [14], a polystyrene (PS) film of initial thickness $h_0 = 240$ nm bonded to a silicon substrate is aligned with high precision (<0.2°) coplanar to the face of a focused ion beam manufactured diamond flat punch of diameter $2a = 2050$ nm. The contact geometry during indentation is shown in Fig. 2(b). Upon application of an axial stress equal to the load divided by the
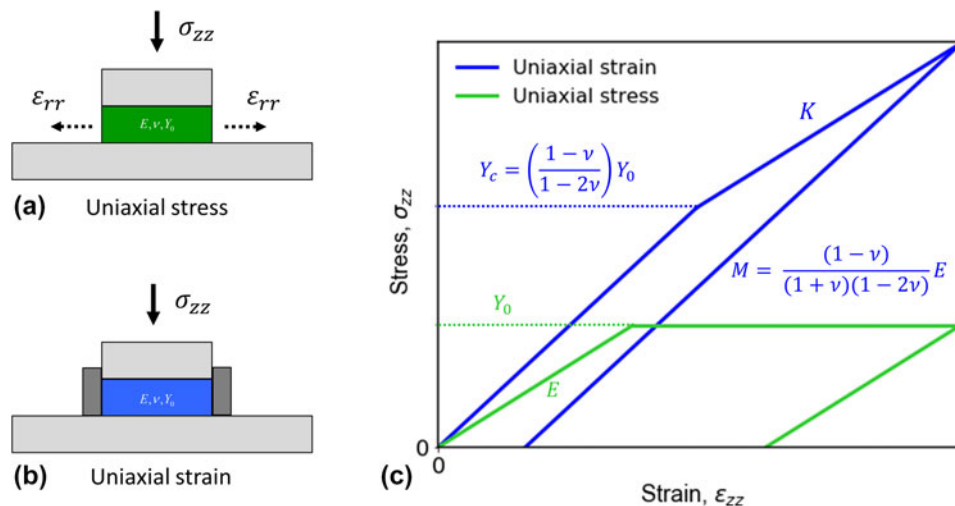
Figure 1: Uniaxial strain mechanics. (a) Two-dimensional representation of the familiar compressive uniaxial stress test. A compressive axial stress σ_{zz} is applied, which results in an axial strain ε_{zz} and radial expansive strain ε_{rr} due to the elastic Poisson effect and plastic flow. (b) Equivalent sketch of the uniaxial strain test. In this case, lateral sample expansion is prevented by a rigid confining jacket (dark gray blocks). With no radial motion possible, the deformation is entirely longitudinal. (c) Stress–strain response of an isotropic linear elastic–plastic material deformed in the two geometries listed above. The elastic response of the uniaxial strain system is stiffer, following the elevated confined elastic modulus M. Yield occurs at a higher confined yield stress Y_c, while plastic loading results in an explicit relationship between stress and strain given by the elastic bulk modulus, K.

contact area $\sigma_{zz} = L/\pi a^2$, the volume beneath the punch becomes laterally constrained through a combination of the film material directly surrounding the contact acting as a confining jacket of finite stiffness and the test aspect ratio $\alpha = 2a/h_0 = 8.5$ rendering deformation largely one dimensional. Figure 2(c) shows the stress–strain (relative displacement, $\varepsilon_{zz} = h/h_0$) curve for indentation of the PS film at a loading rate of 0.2 GPa/s (0.67 mN/s). The curve displays several features of note: first, an initial region of high curvature is observed at very low strain, associated with increasing contact area due to the small residual punch—film misalignment. At high strain, a dramatic change in slope occurs at approximately 0.7 GPa (0.2 strain) corresponding to extrusion flow of material beneath the punch to the surrounding hinterland, followed by an apparent hardening brought about by plastic flow of the polymer in a squeezed geometry. Of significant interest here, however, is the behavior in the low to intermediate strain range of approximately 0.035–0.125 highlighted by the black dotted box and expanded in Fig. 2(d). Within this regime, the response of the film displays the key hallmarks of uniaxial strain identified in Fig. 1(c): two distinct linear slopes separated by a kink at a stress of $\sigma_{zz} = 0.32$ GPa. We assert that our observations of high aspect ratio, well-aligned flat punch indentation of a supported film correspond to uniform, uniaxial strain of a cylindrical puck of film material defined by the punch contact within this region and that the two slopes approximate to the confined elastic modulus M and bulk modulus K, respectively. The kink should therefore demark a sharp division between elastic and inelastic response corresponding to the confined yield stress Y_c.
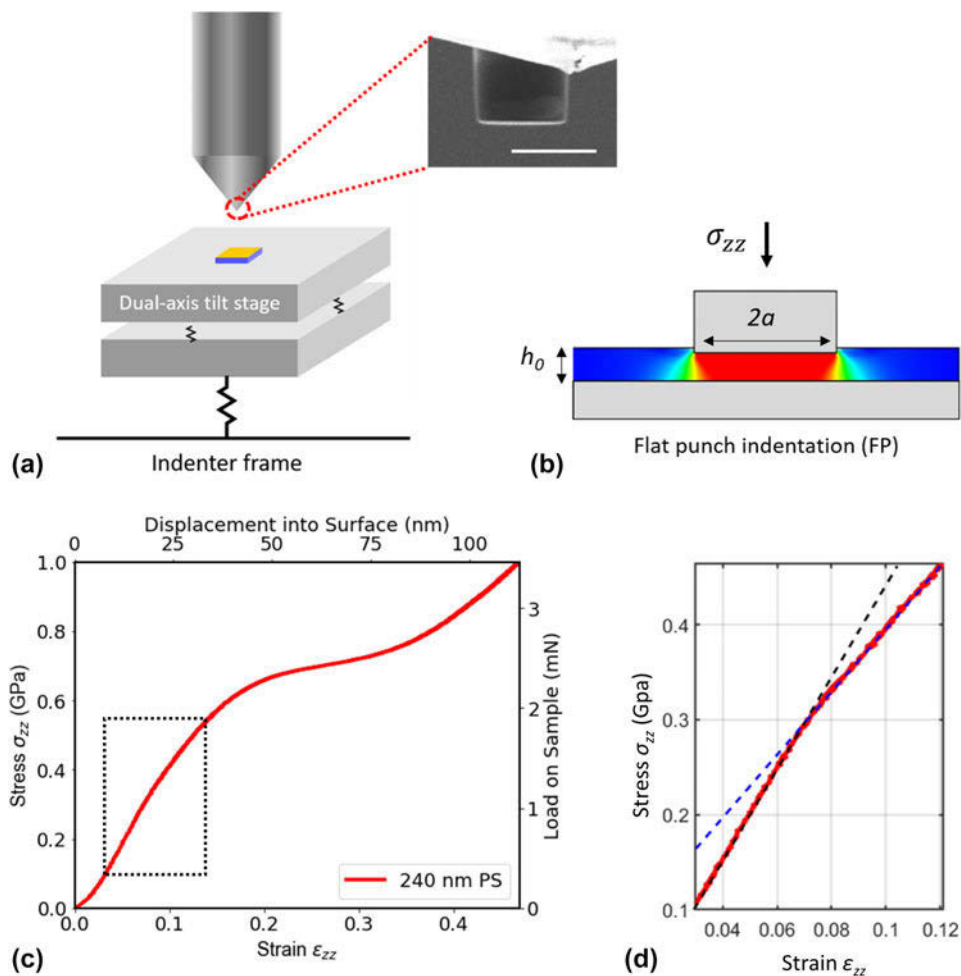

Figure 2: Flat punch indentation of thin films approximates uniaxial strain. (a) Sketch of the flat punch indentation experimental setup. The 2.05 µm diameter diamond flat punch used in this work (inset: scanning electron micrograph, 2 µm scale bar) with schematic of stiff, precision tilt stage system aligning film–substrate system, accuracy <0.2°. (b) Two-dimensional representation of the contact geometry, with the film material surrounding the contact acting as a confining jacket and driving the system toward a state of uniaxial strain. (c) Characteristic load–displacement curve for $h_0 = 240$ nm thick PS film on silicon substrate indented at a punch diameter to film thickness aspect ratio $\alpha = 8.5$. Following an initial region of high curvature due to punch minor misalignment, two linear regions can be observed with sharp kink at $\sigma_{zz} = 0.32$ GPa dividing elastic from inelastic behavior in the pre-extrusion load–displacement curve. (d) Close-up of this region of the curve, which corresponds to loading in a state of uniaxial strain.

To test this assertion, a series of indentations were made to increasing peak stress (0.075 GPa increment) formed in an array of unique locations on a 190 nm PS film bonded to silicon ($\alpha = 10.8$), with the resultant stress–strain curves shown in Fig. 3(a). For uniaxial strain, indents whose peak stress is less than $Y_c \approx 0.3$ GPa should display no residual strain in the x-axis upon unloading to zero stress, while indents to above Y_c should show increasing residual strain due to plasticity with further loading. From Fig. 3(a), it can be seen that this is indeed the case, with residual strain at unload only appearing above Y_c for indents iv–vii, while indents i–iii are fully elastic, apart from some minor hysteresis likely arising as a consequence of glassy polymer viscoelastic dissipation [15]. This is confirmed by atomic force microscopy (AFM) topography images of indents iii–viii taken immediately after indentation, which show that residual deformation manifests only for indents iv and above. Further, radial height profiles of the indentation craters plotted in Fig. 3(c) indicate that the residual deformation is dominated by a uniaxial compactification of the film beneath the punch, with material pileup surrounding the contact area being minimal or entirely absent for indents vi–vii. The lack of volume preserving lateral flow to the surrounding hinterland suggests a permanent longitudinal densification of the indented region as a result of uniaxial strain plasticity. Further loading to a stress greater than ~0.65 GPa results in radial yielding of the

confining film surrounding the contact, leading to a breakdown of the uniaxial strain condition and initiation of lateral flow. This is seen for indent viii, both in the drastic slope change in its stress–strain curve at this stress [Fig. 3(a)] and the large halo of extruded material surrounding the contact [Fig. 3(b)]. However, despite this breakdown, the persistence of stable uniaxial strain deformation to strains approaching 15% makes this technique a unique tool in small scale materials testing. We note that similar results were found for PMMA but are omitted here for the sake of brevity.

The realization of uniaxial strain in flat punch film compression is made possible through two essential features of the geometry: a sufficiently high test aspect ratio α and lateral confinement offered by peripheral film material adjoining the compressed region. As $\alpha \rightarrow \infty$, the deformation must tend toward one dimensional, with the importance of the contact edge region diminished [16]. To demonstrate this, we performed finite element simulations (Abaqus 2019; Dassault Systemes; see Methodology for details) of indentation of a supported layer. In Fig. 4(a), simulated rigid flat punch indentation load versus displacement curves for several contact geometries ($5 \leq \alpha \leq 20$) are shown for a representative glassy polymer film material (simple elastic–plastic constitutive mechanics with $E = 3.0$ GPa, $\nu = 0.33$, $Y_0 = 0.1$ GPa) bonded to a rigid substrate. In Fig. 4(b), this set is reduced to stress versus
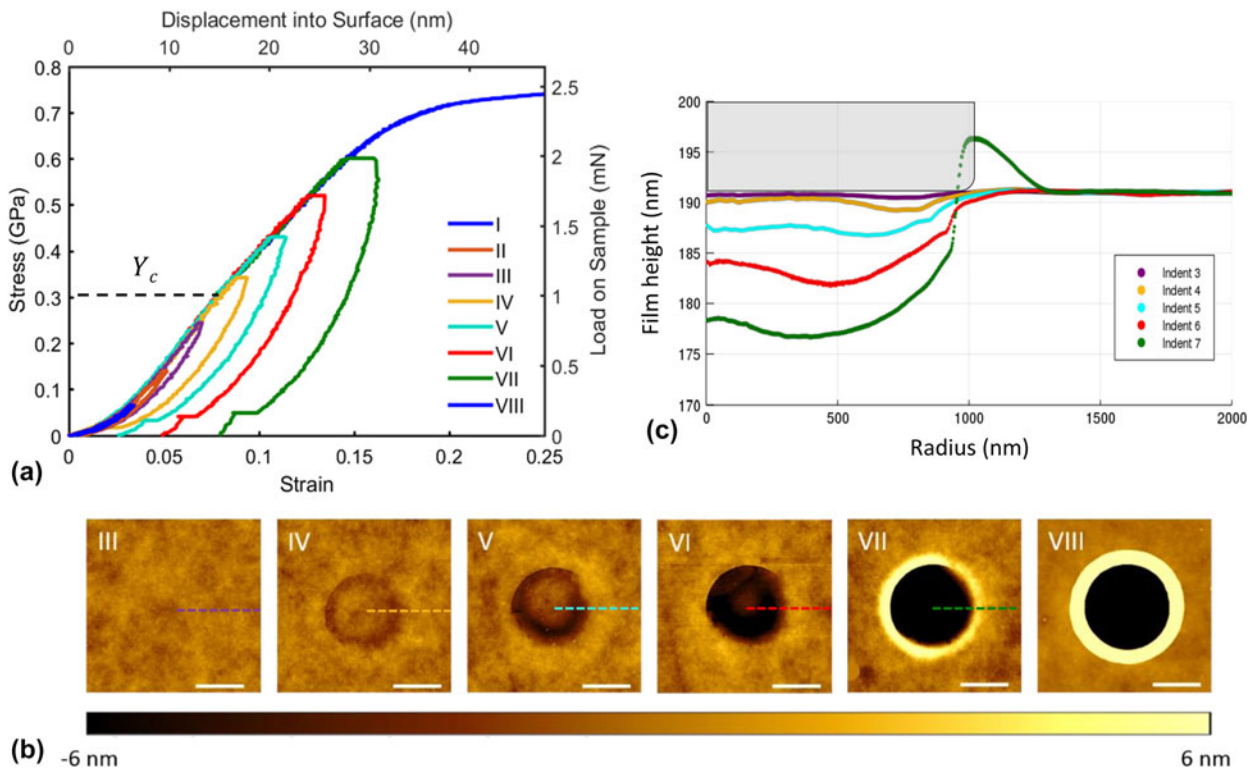
Figure 3: Incremental loading experiments show confined plastic yield. (a) Load–displacement curves for a series of independent intents into 190 nm ($\alpha = 10.8$) PS with incrementing peak load. (b) AFM topography maps of residual strains for indents iii–viii. (c) AFM residual impression profiles for indents iii–vii showing displaced volume.
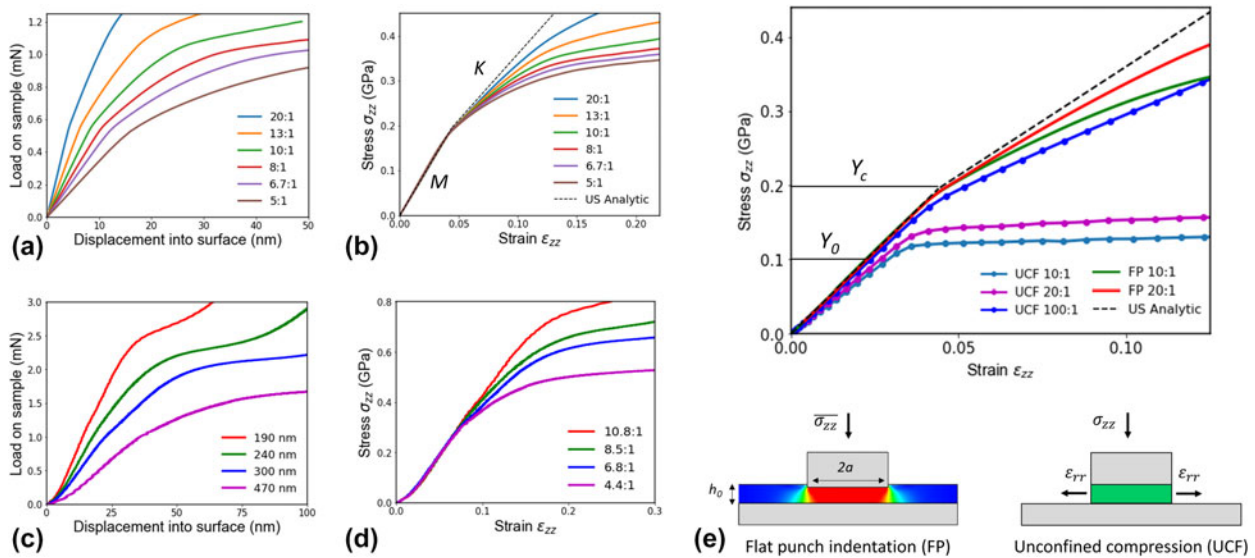
Figure 4: Influence of aspect ratio and lateral confinement on uniaxial strain approximation. (a) FEA-simulated flat punch indentation load–displacement curves for a linear elastic–plastic material with punch to film thickness aspect ratio varied over a range of $5 \leq \alpha \leq 20$. (b) Conversion of these curves to mean stress–relative displacement. At high α, the system tends toward the uniaxial strain solution. (c) Experimental load–displacement data obtained from flat punch indentation of supported PS films with thicknesses ranging from 190 to 470 nm. (d) Conversion of these data to mean stress–relative displacement. The same trend is observed as in (b). (e) Effect of aspect ratio α on the mean stress–relative displacement response of simulated unconfined compression and flat punch indentation systems. While the flat punch geometry approximates well to uniaxial strain at modest α, values on the order of $\alpha = 100$ are required to achieve in the absence of confinement.

strain, with the black dotted line showing the analytic uniaxial strain solution. A complementary set of indentation experiments were performed into PS films of thicknesses 470 nm $\geq$ $h_0 \geq$ 190 nm with the 2050 nm diameter punch ($4.4 \leq \alpha \leq$ 10.8) with load versus displacement and stress versus strain curves shown in Figs. 4(c) and 4(d), respectively. In the simulated case, it was observed that as α increases, the slope of the curve in the confined plastically yielding region tends toward the bulk modulus K as the purity of the uniaxial strain state increases. The same stiffening behavior is observed in the experimental curves in Fig. 4(d). Remarkably, in both cases, the measured constrained elastic modulus M and yield stress Y_c are essentially α invariant over the ranges considered, a feature of great practical value for constitutive parameter extraction. This arises from the effect of lateral constraint provided by the surrounding material, considered in Fig. 4(e), where compression of an unconfined puck is compared with a flat punch on film geometry. Only at very high aspect ratios ($\alpha \sim 100$ or more) does unconfined compression approach uniaxial strain [16, 17], while the surrounding film forms an effective wall at α ~ 10 or less, even though made of constitutively identical material to the compressed puck. This is as prior to yield, only moderate radial stresses are transmitted from the compressed puck to the surrounding film via the elastic Poisson effect. For an elastic–perfectly plastic material, however, once the puck yields shear stress becomes capped at the von Mises yield stress Y_0 and it loses the ability to sustain further shear stress upon additional loading. This in effect causes the deformation to

appear as a material with ν of 0.5, i.e., incompressible elastic, beyond yield. However, the net effect is very different with each strain increment past yield accruing as permanent shape change. The radial stresses acting on the surrounding film increase in accordance with Eq. (1b) and the ability of a film to sustain a confining uniaxial strain condition is lessened.
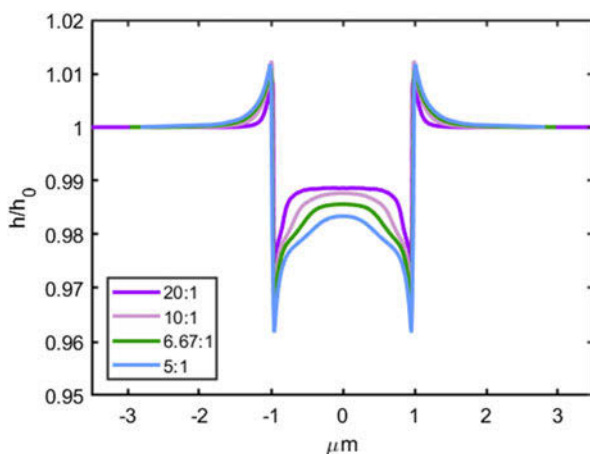
To estimate the conditions necessary to observe yield in our geometry, we consider a two-dimensional polar version of Mott's cavity model [18, 19]. We introduce a constraint factor χ relating yield in simple tension to the yield stress of the wall $Y_w = \chi Y_0$, analogous to Tabor's empirical hardness factor in three-dimensional indentation [18]. In uniaxial strain, yield occurs at an axial stress $\sigma_{zz} = Y_c = Y_0(1 - \nu)/(1 - 2\nu)$, while the stress on the wall is $\sigma_{rr} = \sigma_{zz}\nu/(1 - \nu)$; thus, we require:

$$\nu \leq \frac{\chi}{1 + 2\chi} \quad , \tag{3}$$

as a conservative estimate to observe yield. In two dimensions, $\chi < 3$ and is more than likely between 1 and 2, ranging from low (polymers) to high (metals or ceramics) E/Y_0 ratio, giving an upper ν limit ranging from 0.33 to 0.4. Beyond yield, the elastic component of the strain increment will no longer contain a volume accommodating Poisson effect (i.e., elastic compressibility) implying wall stress increases $\Delta\sigma_{rr}$ should approach $\Delta\sigma_{zz}$. This is consistent with inelastic wall collapse and the onset of extrusion typically observed at stresses of about 1.5–2 times Y_c in Figs. 4(b) and 4(d).

The finite element simulations also provide explanation of the nonuniform residual strains seen in the AFM images and profiles of Figs. 3(b) and 3(c). While the sunken regions toward the edge of the contact area might arise from nonuniform normal stress σ_{zz} of substrate bending, the residual profiles of finite element simulation indents into films bonded to a fully rigid substrate plotted in Fig. 5 show the same characteristic shape. The nonuniformity of the simulated residual strain increases with decreasing aspect ratio α, and the slopes of the stress–strain curves in Fig. 4(b) deviate further from K as α decreases. This suggests that the effect instead arises from finite stiffness and thus imperfect confinement provided by the surrounding film: An elastic stress σ_{rr} from the walls arises across the contact area, causing a slight buckling of the indentation crater as the punch is removed and the system relaxes. This is confirmed by a crater diameter that is slightly smaller than the punch, seen in both simulation and experiment.

With flat punch indentation enabling direct access to intrinsic stress versus strain data via an approximate uniaxial strain state, direct elastic–plastic parameter extraction becomes possible via the relations given in Eqs. (1) and (2). Figure 6(a) shows substrate compliance corrected (see Methodology) stress–strain curves for a 240 nm PS film on silicon obtained with the 2050 nm diameter punch and two other materials, a 280 nm amorphous selenium (aSe) film and a 300 nm PMMA film, both on silicon. These additional films were selected to show the general applicability of the uniaxial strain test for a wide range of glassy materials. aSe typically has a much larger elastic modulus at room temperature than PS and is closer to its glass transition ($T_g \sim 40$ °C) [21, 27], while

PMMA possesses similar elastic properties to PS but has a significantly higher yield stress pressure dependence [20], displays less post-yield strain softening in strain rate controlled testing, and has a substantial secondary beta relaxation at room temperature, which PS does not [21]. Fitted values for M and K for these materials are shown in Fig. 6(b), as well the measured confined yield stress and calculated values for ν and E. These are found to be in broad agreement with literature values obtained via alternative testing methods [22, 23, 24, 25, 26]. The derived Poisson's ratios of 0.38 and 0.39 for PS and PMMA, respectively, are slightly higher than typically reported, approaching that of an incompressible rubber. This is likely due to the significant effect of hydrostatic pressure on the elastic [27] and plastic [20] properties of viscoelastic polymer glasses. Macroscopic tests in confined geometries similar to that presented here have reported values in excess of $\nu = 0.40$ for PMMA [27], indicating that while the parameters extracted here are generally consistent in describing the constitutive behavior of the three materials studied, they serve only as first-order approximations to more complex glassy behavior, where the influence of factors such as loading rate and pressure must be considered.

With direct access to stress–strain data, it is possible to explore more complex constitutive behavior than can be described by linear elastic–plastic mechanics. Figures 6(c) and 6(d) examine the temperature and loading rate dependence of the confined yield stress Y_c for a 170 nm PS film indented under isothermal conditions with a $2a = 1600$ nm flat punch at temperatures in the vicinity of its nominal glass transition ($T_g \approx 100$ °C). Both the confined elastic modulus and bulk modulus are found to decrease as temperature is increased, in keeping with the results of macroscopic longitudinal tensile experiments [17]. The temperature dependence of Y_c is plotted in Fig. 6(e) at loading rates of 0.125 GPa/s (blue) and 0.0125 GPa/s (red). In both cases, a decrease in Y_c on the order of 40% is observed before the T_g region, followed by a rapid decline to zero over a 20 °C range as the material goes from below to above T_g. At the higher loading rate, glassy-like yield behavior is found to persist to temperatures above T_g, consistent with there being less time available for segmental relaxation. Additionally, uniaxial strain deformation implies a hydrostatic pressure field typically on the order of 100 MPa [28], which has been shown to increase T_g by up to 30 °C [29, 30], consistent with the results of Figs. 6(c) and 6(d).

We conclude by noting our results may be significant not only for applications of supported films and coating but also for small scale testing of matter in general. Original nanoindentation experiments that accessed small volumes but had results obscured by large strain gradients have been clarified by realizing uniform compression of slender micropillars prepared by direct micromachining of the sample [7]. However, for
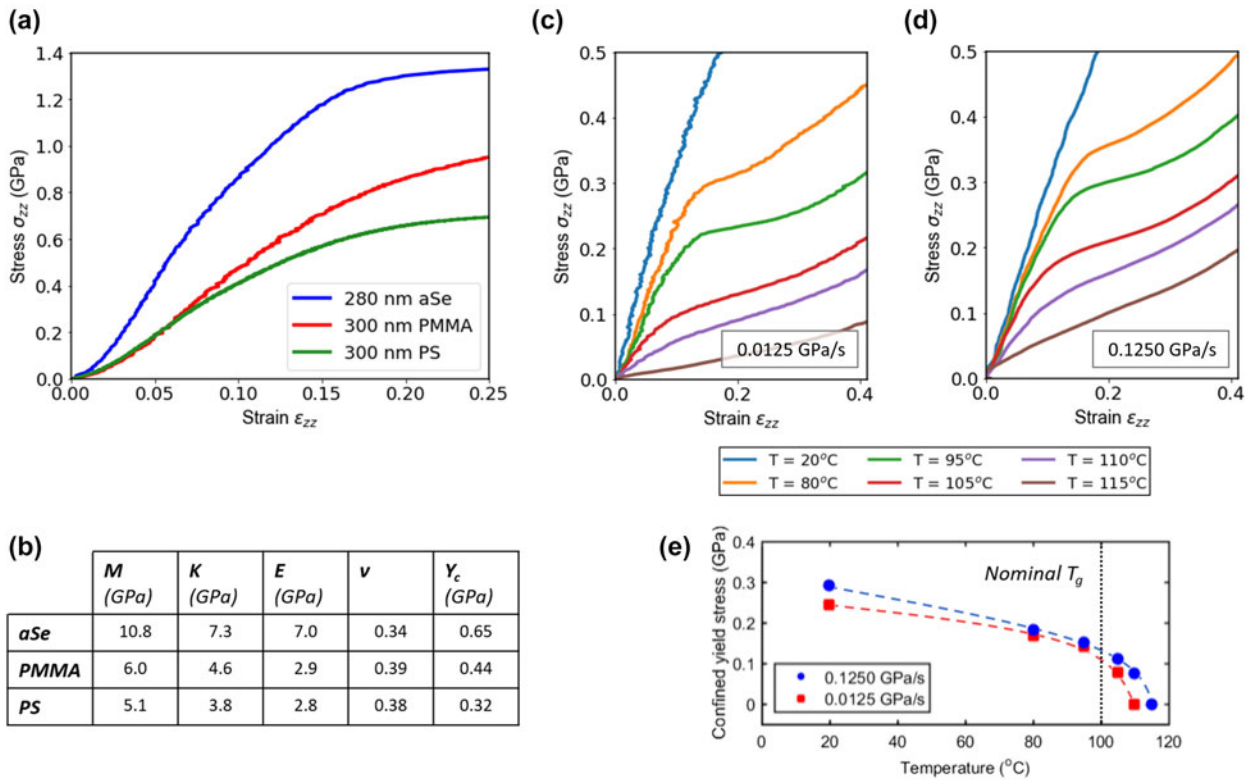

Figure 5: Residual deformation profiles for finite element simulation of flat punch indentation. Profiles were obtained following simulated indentation into films of the elastic–plastic material bonded to a rigid substrate, spanning an aspect ratio $5 \leq \alpha \leq 20$. A buckling-like nonuniformity of the residual profiles increases with decreasing α, which is ascribed to elastic relaxation of the film surrounding the contact. Residual height is normalized to the initial film thickness h_0, all indents were performed to 0.075 strain.

Figure 6: Parameter extraction via uniaxial strain indentation. (a) Stress–strain curves for amorphous selenium (blue), PMMA (red), and PS (green) supported films on silicon. (b) Extracted elastic parameters and confined yield stress. (c) Elevated temperature stress–strain curves for a 170 nm PS film indented with a 1600 nm diameter silicon punch at a 0.0125 GPa/s loading rate. (d) Same curves for a 0.1250 GPa/s loading rate. (e) Confined yield stress as a function of indentation temperature at two loading rates. Yield is observed at temperatures substantially higher than the nominal glass transition.

materials exhibiting inhomogeneous deformation behavior at larger strains (e.g., shear bands), geometric effects with loss of stability can arise under load control typical of nanomechanical instrumentation that again obscure intrinsic behavior. We thus see a complementary nature of the "confined layer compression" we introduce here, which allows mechanically rigorous investigation of stiffly supported, soft materials such as free volume glasses in the post yield region while maintaining a known geometry and dynamic stability.

Methodology

Sample preparation

PS thin films (Polymer Source Inc.) of 1.13 MDa molecular weight and polydispersity ≈1 of thicknesses ranging from 190 to 670 nm were prepared via spin coating from PS /toluene solutions (1–3 wt% PS) on silicon $\langle 100 \rangle$ wafer pieces of approximately 1 cm^2 (University Wafer). Samples were then heated to T_g + 30 °C (130 °C) for 30 min on a hotplate (Torrey Pines Scientific) to remove residual solvent content, before being stored under vacuum overnight. Film thickness was measured via profilometry using a Veeco Dektak 6M profilometer with sub nanometer accuracy and confirmed via AFM.

Fabrication of amorphous selenium samples

The amorphous selenium (aSe) used in the current work was made from an initial material that came in the form of pellets having a purity of 99.999%. The selenium films were produced by the procedures described in Ref. 25. Physical vapor deposition was used to deposit 280 nm thick selenium films on to silicon wafer substrates under 10^{-7} torr vacuum conditions using a Varian high vacuum evaporator (Varian 3118). The films were deposited at room temperature (23 °C) with deposition rate of 0.1 nm/s. The film thickness was determined by following O'Connell and McKenna's procedures [31], in which the deposited aSe films were gently scored, and the step height was measured using an AFM (Keysight Technology SPM 5500).

Flat punch indentation experiments

A diamond flat punch of 2050 nm diameter was manufactured via focused ion beam milling of a conventional cube corner indenter tip (Micro Star Technologies) using an FEI Strata 235 dual-beam FIB-SEM system, as described previously [14]. Samples were mounted to the indenter tilt stage (Physik Instrumente M-044) via crystal bond (Electron Microscopy

Sciences). Indentations were performed using an MTS Nano-indenter XP system equipped with the low-load dynamic contact module. Alignment was ensured between punch and sample via AFM scans of residual indentation impressions using a DME DS 95 in tapping mode and tilt stage correction [14, 32]. Indents were performed at a constant loading rate of 0.67 mN/s, corresponding to a stress rate of 0.20 GPa/s. A 1 nm vertical oscillatory displacement was applied to the punch at 45 Hz throughout loading. Prior to indentation, thermal drift was measured to be no greater than 0.05 nm/s for all experiments. During unloading, drift was again measured, with the tip held on the surface at 10% peak load for 60 s, and any subsequent displacements were subtracted. All experiments were conducted under ambient conditions, except for elevated temperature indentation studies. High-resolution AFM topography scans were performed on the 190 nm film [Figs. 1(e)–1(g)] using a Bruker MultiMode 8-HR in tapping mode, equipped with Adama super-sharp tips ($r_{tip} \sim 5$ nm). All scans were made within 5 days of indentation.

Stiffness correction

Flat punch indentation stiffness k measured at zero strain for a supported elastic layer has been modeled as a combination of springs and related to an effective reduced modulus E_{eff}^* [33, 34]. Compression stiffness of the constrained puck in series with half-space indentation stiffness of the substrate gives:

$$k = 2aE_{eff}^* = E \cdot \frac{\pi C_w C_s}{4(C_w/S + C_s/\alpha)} \quad , \qquad (4)$$

where $S = E_s/E$ is the ratio of substrate to film Young's moduli, and C_s and C_w are fitting parameters accounting for elastic bending of the substrate and the wall of material confining the compressed puck, respectively. These fitting parameters

nominally depend on specific values of S and α and Poisson's ratio and friction conditions. For measuring constitutive behavior at finite strain including inelastic effects, we expect a qualitatively similar condition but with potential dependence on modulus to yield stress ratio.

The experimentally measured displacement of the punch combines motion into the film as well as bending of the substrate and instrument. The nanoindenter (MTS DCM) gantry frame had a stiffness of 2 mN/m. The dual-axis tilt-stage (Physik Instrumente) was determined to have a maximum 490 ± 10 kN/m stiffness in the sample mounting region using deep Berkovich tip indentations with Nanoindenter XP head (6 mN/m frame stiffness.)

The combined effect of the finite substrate and instrument frame stiffness was accounted for by performing flat punch indentation of an exposed portion of the silicon substrate supporting each film (formed by scraping film with plastic spatula to expose a small area) to a peak load of approximately 8 mN. Once in full contact, stiffness was found to be constant with depth of indentation, typically within the range of 100,000–120,000 N/m. The variation depended on macroscopic sample placement on the tilt stage. An example of stiffness determination used for the experiments reported in Fig. 6 is shown in Fig. 7, where both direct quasi-static indentation over a period of 10 s and small amplitude (1 nm) dynamic oscillation at 75 Hz were used to measure stiffness. The dynamic stiffness of 115 ± 3 kN/m agrees well with the quasi-static unload slopes 120 ± 3 kN/m and 116 ± 3 kN/m at two indentation positions.

This stiffness was used to approximate the total stiffness of substrate, indenter frame, and support gantry designated k_{frame}. By considering the indentation geometry as one-dimensional in the limit of high S/low α (polymers on silicon) true displacement of the punch into the surface was determined from
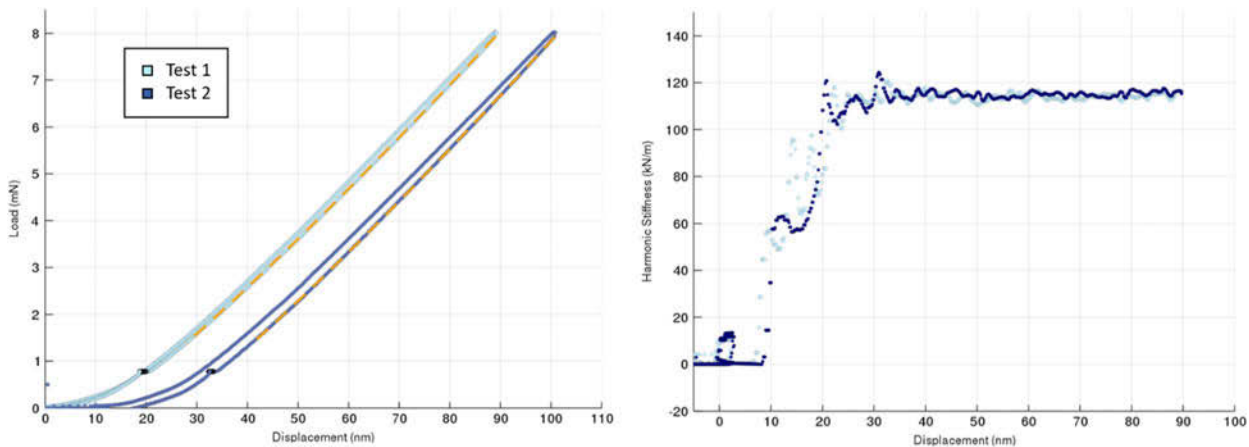
Figure 7: Determination of substrate and instrument stiffness by diamond flat punch indentation. Quasi-static unload fits with slopes 120 kN/m and 116 kN/m for tests 1 and 2 (latter plotted with 10 nm offset for clarity), respectively, at point of unload (yellow dotted lines, left) agree well with 115 kN/m dynamic stiffness observed once punch comes into full contact at 30 nm (right). Note lack of dynamic stiffness dependence with depth once contact established.

measured displacement via $d_{\text{true}} = d_{\text{total}} - L/k_{\text{frame}}$, where we have assumed that k_{frame} is independent of indentation depth for strains less than 10%. As load is equal for all one-dimensional spring elements in series, no correction was required for the load signal. We note that this one-dimensional stiffness correction serves only as a first-order approximation, best applied to instances of compliant materials on stiff substrates. The effects of substrate/punch bending for more rigid film materials will cause deviations from the pure uniaxial strain state, particularly at high punch to film aspect ratio where the stiffness of the contact scales as $k \propto 1/h_0$ [35]. We have performed comprehensive simulations incorporating substrate compliance (to be reported in a future publication), indicating that provided $S > 50$ and $\alpha > 5$, the response remains within 5% of uniaxial strain well past yield.

Finite element simulations

Axisymmetric simulations of flat punch indentation were performed using ABAQUS Explicit finite element package (2018 and 2019; Dassault Systemes). The punch was modeled as a perfectly rigid body of 2 μm diameter with a radius of curvature of 50 nm at each corner. This value was chosen to reflect the finite sharpness of the punch's edges produced experimentally via FIB milling and to aid in the simulation process by lessening the degree of stress concentration.

For the results in Fig. 4, the film was modeled as an elastic–perfectly plastic material with $E = 3.0$ GPa, $\nu = 0.33$, $Y_0 = 0.1$ GPa, and $\rho = 1.04$ g/cm^3. These values were chosen to reflect a typical glassy polymer. The width of the film was set at 40 μm. Four-node bilinear axisymmetric quadrilateral (CAX4R) elements were utilized, with the initial element area set as 10×10 nm^2 for all film thicknesses. Indentation is simulated via prescribing a vertical displacement of the punch face. No other displacements of the punch are allowed. A full-slip condition is specified between film surface and film, save for the punch–film interface friction simulations reported in Fig. 2(h), where a static coefficient of friction was introduced. An encastre condition was applied to the bottom surface of the film, allowing no displacements and therefore simulating a full-stick condition on a rigid substrate. Load–displacement curves were produced via tracking the displacement and vertical reaction forces on a reference point at the center of the punch. Reaction forces were converted to stresses by dividing by the average contact area, corresponding to a diameter of 1950 nm when punch rounding was subtracted. Displacements were converted to engineering strain by dividing by the initial film thickness.

Author contributions

OB, JdS, and WCO conducted indentation experiments. OB, MC, and GLWC performed finite element simulations. OB, JBP, and GLWC wrote the manuscript.

HY performed vapor deposition experiments and edited the manuscript. GBM worked with HY and coordinated the aSe sample sharing with GLWC. GBM also edited the manuscript.

Competing interests

The authors declare no competing interests.

Data and materials availability

All data are available in the main text or the supplemental materials. For additional queries, please contact the corresponding author.

Supplementary material

To view supplementary material for this article, please visit https://doi.org/10.1557/jmr.2020.42.

References

1. **M. Alcoutlabi and G.B. McKenna**: Effects of confinement on material behaviour at the nanometre size scale. *J. Phys.: Condens. Matter* **17**, R461–R524 (2005).

2. **H.D. Rowland, W.P. King, J.B. Pethica, and G.L.W. Cross**: Molecular confinement accelerates deformation of entangled polymers during squeeze flow. **322**, *Science*. 720–724 (2008).

3. **W.C. Oliver and G.M. Pharr**: An improved technique for determining hardness and elastic modulus using load and displacement sensing indentation experiments. *J. Mater. Res.* **7**, 1564–1583 (1992).

4. **J.B. Pethica, R. Hutchings, and W.C. Oliver**: Hardness measurement at penetration depths as small as 20 nm. *Philos. Mag. A* **48**, 593–606 (1983).

5. **R. Saha and W.D. Nix**: Effects of the substrate on the determination of thin film mechanical properties by nanoindentation. *Acta Mater.* **50**, 23–38 (2002).

6. **G.M. Pharr and W.C. Oliver**: Measurement of thin film mechanical properties using nanoindentation. *MRS Bull.* **17**, 28–33 (1992).

7. **M.D. Uchic, D.M. Dimiduk, J.N. Florando, and W.D. Nix**: Sample dimensions influence strength and crystal plasticity. *Science* **305**, 986–989 (2004).

8. **C.M. Stafford, C. Harrison, K. Beers, K. Alamgir, E. Amis, M.R. Vanlandingham, H.C. Kim, W. Volksen, R.D. Miller, and E. Simonyi**: A buckling-based metrology for measuring the elastic moduli of polymeric thin films. *Nat. Mater.* **3**, 545–550 (2004).

9. **P.A. Connell and G.B. McKenna**: Rheological measurements of the thermoviscoelastic response of ultrathin polymer films. *Science.* **307**, 1760–1763 (2005).

10. **G. Mavko, T. Mukerji, and J. Dvorkin**: *The Rock Physics Handbook* (Cambridge University Press, Cambridge, England, 2009); pp. 22–23.

11. **R.O. Davies and A.P.S. Selvadurai**: *Plasticity and Geomechanics* (Cambridge University Press, Cambridge, England, 2005); p. 44.

12. **Z. Ma and K. Ravi-Chandar**: Confined compression: A stable homogeneous deformation for constitutive characterization. *Exp. Mech.* **40**, 38–45 (2000).

13. **K. Ravi-Chandar and Z. Ma**: Inelastic deformation in polymers under multiaxial compression. *Mech. Time-Dependent Mater.* **4**, 333–357 (2000).

14. **G.L.W. Cross, B.S. O'Connell, J.B. Pethica, H. Rowland, and W.P. King**: Variable temperature thin film indentation with a flat punch. *Rev. Sci. Instrum.* **79**, 013904 (2008).

15. **A.S. Argon**: *The Physics of Deformation and Fracture of Polymers* (Cambridge University Press, Cambridge, England, 2013); p. 112.

16. **G. Lindsey, R.A. Schapery, M.L. Williams, and A.R. Zak**: The triaxial tension failure of viscoelastic materials, Internal report, US Aerospace Research Laboratories. (Pasedena, California, September 1963).

17. **J.W. Kim, G.A. Medvedev, and J.M. Caruthers**: Observation of yield in triaxial deformation of glassy polymers. *Polymer* **54**, 2821–2833 (2013).

18. **K.L. Johnson**: *Contact Mechanics* (Cambridge University Press, Cambridge, England, 1985); p. 171.

19. **K.L. Johnson**: The correlation of indentation experiments. *J. Mech. Phys. Solids* **18**, 115–126 (1970).

20. **R. Quinson, J. Perez, M. Rink, and A. Pavan**: Yield criteria for amorphous glassy polymers. *J. Mater. Sci.* **32**, 1371–1379 (1997).

21. **C.B. Roth**: *Polymer Glasses* (CRC Press, Boca Raton, 2016); pp. 31, 161.

22. **R. Böhmer and C.A. Angell**: Elastic and viscoelastic properties of amorphous selenium and identification of the phase transition between ring and chain structures. *Phys. Rev. B* **48**, 5857–5864 (1993).

23. **J. Brandrup, E.H. Immergut, and E.A. Grulke**: *Polymer handbook* (Wiley-Interscience, New Jersey, 1999).

24. **P.H. Mott, J.R. Dorgan, and C.M. Roland**: The bulk modulus and Poisson's ratio of "incompressible" materials. *J. Sound Vib.* **312**, 572–575 (2008).

25. **H. Yoon and G.B. McKenna**: Dynamic and temperature dependent response of physical vapor deposited Se in freely standing nanometric thin films. *J. Chem. Phys.* **144** (2016).

26. **K.M. Bernatz, I. Echeverría, S.L. Simon, and D.J. Plazek**. Characterization of the molecular structure of amorphous selenium using recoverable creep compliance measurements. *J. Non-Cryst. Solids* **307–310**, 790–801 (2002).

27. Online Source: **D.R. Stephens, H.C. Heard, and R.N. Schock**: High-pressure mechanical properties of polymethylmethacrylate (1972). Available at: https://www.osti.gov/servlets/purl/4249322.

28. **O. Brazil**: Deformation and yield of polymer thin films under confinement. Thesis (Trinity College Dublin, Dublin 2, Ireland, 2019).

29. **A. Quach and R. Simha**: Pressure-volume-temperature properties and transitions of amorphous polymers; polystyrene and poly(orthomethylstyrene). *J. Appl. Phys.* **42**, 4592–4606 (1971).

30. **H-J. Oels and G. Rehage**: Pressure-volume-temperature measurements on atactic polystyrene. A thermodynamic view. *Macromolecules* **10**, 1036–1043 (1977).

31. **P.A.O. Connell and G.B. Mckenna**: Novel nanobubble inflation method for determining the viscoelastic properties of ultrathin polymer films. *Rev. Sci. Instrum.* **78**, 013901 (2012).

32. **H.D. Rowland, W.P. King, G.L.W. Cross, and J.B. Pethica**: Measuring glassy and viscoelastic polymer flow in molecular-scale gaps using a flat punch mechanical probe. *ACS Nano* **2**, 419–428 (2008).

33. **M.J. Wald, J.M. Considine, and K.T. Turner**: Determining the elastic modulus of compliant thin films supported on substrates from flat punch indentation measurements. *Exp. Mech.* **53**, 931–941 (2013).

34. **M.J. Wald, J.M. Considine, and K.T. Turner**: Measuring the elastic modulus of soft thin films on substrates. *Exp. Appl. Mech.* **6**, 741–747 (2011).

35. **G.L.W. Cross, B.S. O'Connell, and J.B. Pethica**: Influence of elastic strains on the mask ratio in glassy polymer nanoimprint. *Appl. Phys. Lett.* **86**, 1–3 (2005).